

## Radial shearing dynamic wavefront sensor based on a geometric phase lens pair

HYO MI PARK,<sup>1</sup> DAEWOOK KIM,<sup>2</sup> CHARLOTTE E. GUTHERY,<sup>2</sup> AND KI-NAM JOO<sup>1,\*</sup>

<sup>1</sup>Department of Photonic Engineering, Chosun University, 309 Pilmun-daero, Dong-gu, Gwangju 61452, Republic of Korea

<sup>2</sup>Wyant College of Optical Sciences, University of Arizona, 1630 E. University Blvd., Tucson, Arizona 85721, USA

\*Corresponding author: knjoo@chosun.ac.kr

Received 1 November 2021; revised 7 December 2021; accepted 12 December 2021; posted 15 December 2021; published 21 January 2022

**A radial shearing dynamic wavefront sensor is theorized and experimentally verified. The proposed sensor is based on a geometric phase lens pair that generates two radially sheared wavefronts. A polarization pixelated camera instantaneously obtains polarization-multiplexed phase maps from a single acquired image using a spatial phase-shifting technique. Experimental tests applied several wavefront shapes with a deformable mirror. The results were compared with a Shack–Hartmann wavefront sensor to evaluate the performance.** © 2022 Optica Publishing Group

<https://doi.org/10.1364/OL.447505>

The importance of wavefront sensing has significantly increased in applications of adaptive optics for astronomy and extreme ultraviolet (EUV) lithography [1]. Wavefront sensors are also widely used to test optical components of smartphone cameras, as well as virtual reality (VR) and augmented reality (AR) devices [2,3]. Two conventional methods of measuring wavefront shapes are with a Shack–Hartmann wavefront sensor (SHWS) [4] or a pyramid wavefront sensing technique [5]. These sensors have a high sensitivity and robust response but are lacking in lateral resolution and dynamic range. As an alternative to wavefront metrology, an optical interferometer can be used to improve the lateral resolution of measurements. Several interferometric principles have been proposed and experimentally verified, such as point diffraction interferometry [6], digital holography [7], lateral shearing interferometry [8], and radial shearing interferometry [9,10]. Among these, the radial shearing interferometer (RSI) has the benefit of reconstructing a wavefront using a single radially sheared interferogram with no reference wavefront. A cyclic RSI (CRSI) has the advantage that there is a common path between the two sheared beams, which results in a highly stable system that is immune to vibrations [10].

Compared to typical RSIs, a wavefront sensor must be more compact and flexible to facilitate instantaneous and dynamic measurements of time-varying wavefronts. In conventional RSIs, the radial shearing ratio is difficult to change; it is only adjustable by replacing optical components or using a sophisticated zoom lens system [9]. The optical configuration is quite bulky and complex for generating radially sheared beams and obtaining phase maps [9,10].

Recently, a geometric phase optical component has been introduced and applied in shearing interferometry. The operation principle of using this component in an RSI was introduced from a manufacturing point of view [11]. In order to apply this concept to a real-world application, the theoretical and practical development of a phase extraction method is essential. An instantaneous phase extraction solution will enable the metrology of time-varying dynamic wavefronts. To achieve wavefront sensing based on the properties of a geometric phase lens (GPL), the properties of the instrument must be selected carefully to fully exploit the benefits of a snapshot wavefront sensor.

In this Letter, we propose a polarization-multiplexed radial shearing wavefront sensor (RSWS) that uses a GPL pair. Two radially sheared beams are generated by the characteristics of a GPL, and the phase map can be instantaneously obtained using a polarization pixelated CMOS camera (PCMO) without any moving components. Figure 1 shows the optical configuration of the RSWS in this investigation, which involves the use of a GPL pair to generate two radially sheared wavefronts and a PCMO to obtain four phase-shifted interferograms from a single image. When a linearly polarized wavefront is incident to the GPL pair, two radially sheared wavefronts are generated with the two orthogonal circular polarizations. Then, two circularly polarized wavefronts are combined by the polarization array inside the PCMO, which can generate four phase-shifted interferograms [12]. Using the spatial phase-shifting technique, the phase map is instantaneously calculated, and the original wavefront is obtained by a reconstruction algorithm [13,14].

A GPL is a lens with polarizing characteristics. It affects light differently depending on the incident polarization state, as illustrated in Fig. 2(a). An incident beam that is collimated and right-handed circularly polarized (RHP) will converge after a single GPL and convert into left-handed circularly polarized (LHP) light. A collimated LHP beam will diverge and convert into RHP light. When the incident collimated beam is linearly polarized (LP), it is divided into two beams based on circular polarization: a focused LHP wavefront and its RHP diverging conjugate. A second GPL is placed downstream, as shown in Fig. 2(b), such that both the focused and diverging beams are semi-collimated and radially sheared. The polarization states of the two beams are the same as that originally incident on the first GPL. Based on the polarization characteristics of the

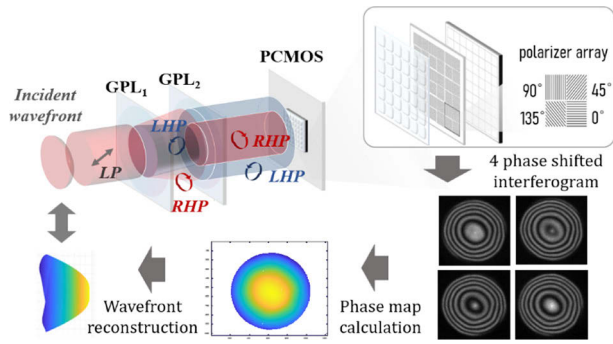


**Fig. 1.** Schematic of the proposed radial shearing wavefront sensor that uses a GPL pair and a polarization pixelated CMOS camera (PCMOS). The linear polarization (LP) of the incoming wavefront is split into left-handed circular polarization (LHP) and right-handed circular polarization (RHP) for measurements. The top-right inset describes the inner polarizer array of the PCMOS.

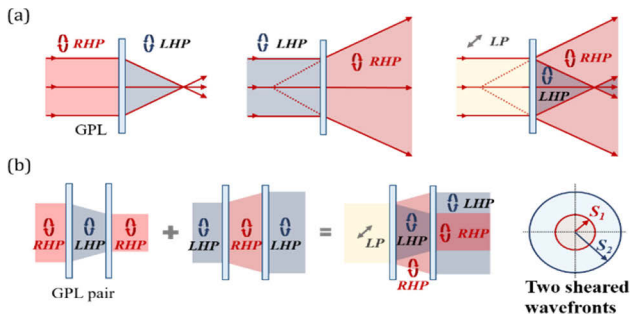


**Fig. 2.** (a) Characteristic responses of a GPL to RHP, LHP, and LP incident light. (b) Characteristic response of a GPL pair and the radial shearing effect in response to an incident LP wavefront.

GPL, the larger beam will be LHP and the smaller inset will be RHP.

The radial shearing ratio between the two beams is tunable by altering the separation of the two GPLs and their focal lengths. Ray transfer matrices are used to mathematically describe the radial shearing and the transfer functions  $T$  of the two beams, expressed as

$$T_{RHP,LHP} = \begin{pmatrix} 1 \mp \frac{d}{f_1} & d \\ \frac{1}{f_2} - \frac{d}{f_1 f_2} - \frac{1}{f_1} & 1 \pm \frac{d}{f_2} \end{pmatrix}, \quad (1)$$

where  $f_1$  and  $f_2$  are the focal lengths of  $GPL_1$  and  $GPL_2$  and  $d$  is the separation distance between them. It should be noted that the operators in the first and the fourth components depend on whether the incident light is RHP or LHP. If  $f_1$  and  $f_2$  are the same focal length  $f$ , which is much larger than  $d$ , Eq. (1) can be simplified as follows:

$$T_{RHP,LHP} = \begin{pmatrix} 1 \mp \frac{d}{f} & d \\ -\frac{d}{f^2} & 1 \pm \frac{d}{f} \end{pmatrix} \cong \begin{pmatrix} 1 \mp \frac{d}{f} & d \\ 0 & 1 \pm \frac{d}{f} \end{pmatrix}, \quad d \ll f. \quad (2)$$

From Eq. (2), the radial shearing ratio  $s$  for an incident ray, defined as a vector of height  $r$  and direction angle  $\theta$ , can be

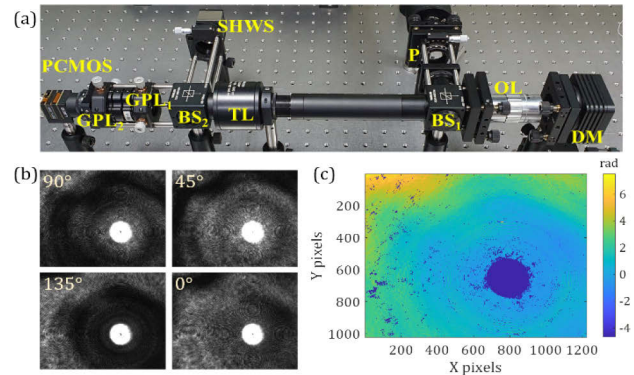


**Fig. 3.** (a) Photograph of the experimental setup, including the linear polarizer (P) for the incident beam, tube lens (TL), objective lens (OL), and DM to condition the tests. Both a SHWS and a RSWS, separated by a beam splitter (BS), were used for wavefront estimation. The RSWS comprised a GPL pair and a PCMOS. (b) Four phase-shifted interferograms from the PCMOS. (c) Calculated unwrapped phase of the setup with a flat DM.

derived as

$$s = \frac{\left(1 - \frac{d}{f}\right)r + d\theta}{\left(1 + \frac{d}{f}\right)r + d\theta} = \frac{(f-d)r + fd\theta}{(f+d)r + fd\theta}. \quad (3)$$

As shown in Eq. (3),  $s$  is a function of the beam size  $r$  and the ray angle of the incident wave  $\theta$ . In the case where  $r \gg f\theta$ ,  $fd\theta$  in Eq. (3) can be ignored, leading to

$$s = \frac{f-d}{f+d}, \quad r \gg f\theta. \quad (4)$$

This can be used beforehand to determine the radial shearing ratio from the separation and focal length of the GPL pair. Furthermore, the ratio can easily be adjusted by moving one of the GPLs along the optical axis, i.e., by changing  $d$ .

To experimentally verify the instantaneous phase-shifting capability for dynamic wavefront metrology, an optical system for the RSWS was assembled, as shown in Fig. 3(a). Various target wavefronts were applied using a 40-actuator piezo deformable mirror (DM) from Thorlabs. The GPL pair comprised two 75-mm-focal-length GPLs from Edmund Optics. The pair were separated by 0.4 mm. This small distance was the measured thickness of the GPL, and was achieved by contacting the two surfaces. Although the radial shearing ratio could be adjusted by changing  $d$ , the GPL pair was conveniently aligned by contacting the two surfaces. This is a valid strategy so long as the shearing ratio is small according to the definition of an RSI. The radial shearing ratio  $s$ , as described by Eq. (3), was then set to 0.989. An infinity-corrected microscope with a  $2\times$  objective and a PCMOS from Lucid Vision Labs were used to image the four phase-shifted interferograms. A Thorlabs SHWS was used to cross-check the RSWS measurements by imaging the same wavefront at the same time. The two measurement planes were conjugated to the target surface. A supercontinuum laser from NKT photonics was the light source. The light was centered at 550 nm and had a 10 nm FWHM bandwidth. This was the wavelength that the GPLs were designed to image.

Four phase-shifted interferograms, as shown in Fig. 3(b), were obtained with the PCMOS. Any additional measured unwrapped

phase images were calculated with respect to the flat DM, as shown in Fig. 3(c). The flat phase map was not null due to the wavefront error in the incident beam and the DM flat errors. Additionally, the wavefront may suffer due to fabrication errors in the optics of the imaging system. This intrinsic system error was used for calibration by subtracting the flat phase in Fig. 3(c) from any measured results. The saturated region of the interferogram was caused by the leakage of zero-order portions of the beam, which are not diffracted by the GPLs, into the final image. A GPL pair specifically designed for this project would significantly reduce this issue.

The DM was operated to add variable amounts of defocus by gradually changing from a concave to a convex surface. The PCMOs captured the instantaneous interferograms for each applied shape and recorded a corresponding phase map. The systematic error was compensated for using the flat DM phase from Fig. 3(c). Each wavefront was estimated using a modal method reconstruction based on Zernike polynomials [14]. In this method, the applied wavefront is expressed as a Zernike polynomial, so the phase recorded by the RSWS will be a function of Zernike polynomials. The coefficients are estimated using a regression technique. For these experiments, the resolution of the DM set the limit of reconstruction to Zernike polynomials of radial order four. Thirty wavefronts with varying amplitudes of defocus were reconstructed, and the results are shown in Fig. 4(a). Any tilt in the individual wavefront was eliminated with the DM. The reconstructed wavefront matched the applied shape well, gradually varying from concave to convex, as expected. The measured results from the SHWS, which were obtained using the same procedure involving the reconstruction and removal of systematic errors, closely matched the estimations from the RSWS. Each radius of curvature (ROC)

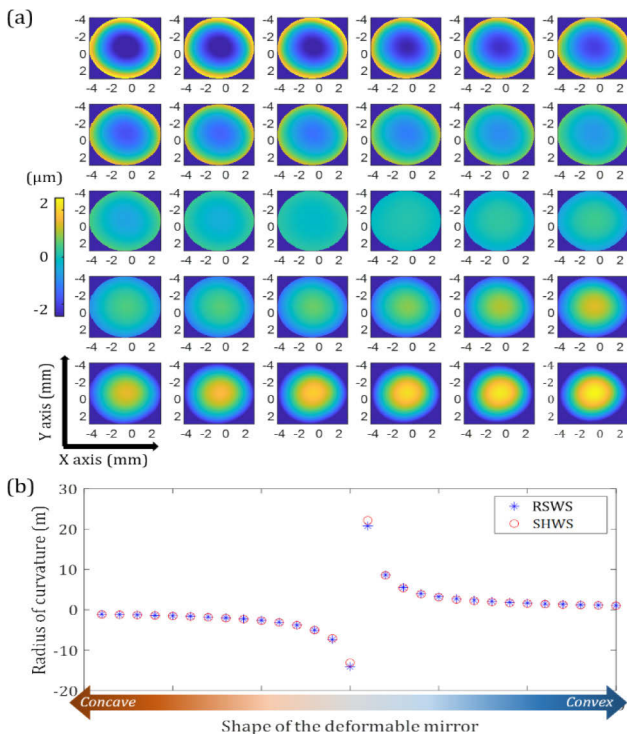


**Fig. 4.** (a) Reconstructed wavefronts of concave (upper left) to convex (bottom right) wavefronts applied with the DM, as obtained using the RSWS. (b) Comparison of the radii of curvature estimated with the RSWS and the SHWS from benchtop system tests.

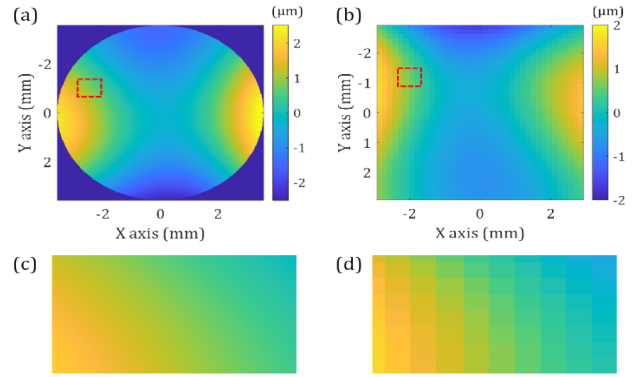


**Fig. 5.** Estimated wavefronts from the (a), (c) RSWS and (b), (d) SHWS in response to secondary astigmatism. (c) and (d) are enlarged views of the wavefront sections indicated in (a) and (b).

was compared with a sphere fitting technique, and the resulting measurements are shown in Fig. 4(b). The differences between the two sensors were less than 1.5%.

To further verify the dynamic performance of the RSWS, higher-order wavefront estimations were compared to those from the SHWS. Secondary astigmatism was applied with the DM, and the corresponding wavefront was measured by both sensors, as shown in Fig. 5. The sensors were slightly misaligned, so that the relative measurement was off-center, but the overall effect is still clearly visible. Reconstruction produced the secondary astigmatism shape at roughly the same magnitude for both sensors. The resolution of the RSWS was much higher than that of the SHWS, as demonstrated by Figs. 5(c) and 5(d). This is because the micro-lens array limits the sampling rate of the SHWS, while the RSWS images very dense radial shearing interferograms directly on the PCMOs. This also shows that the RSWS can reconstruct a wavefront with a higher lateral resolution than the SHWS. Moreover, the most beneficial feature of the RSWS is its ability to instantaneously measure changes in the wavefront over time with a snapshot technique. To monitor this effect, the DM is continuously switched between several different Zernike aberrations, as shown in Fig. 6. For this test, the RSWS measured each wavefront within a 0.1 s time interval. The measurement speed is determined solely by the frame rate of the PCMOs, as no additional temporal procedures are needed to complete reconstruction.

The RSWS can be operated without any significant consideration of the radial shearing ratio or the quadratic phase in the

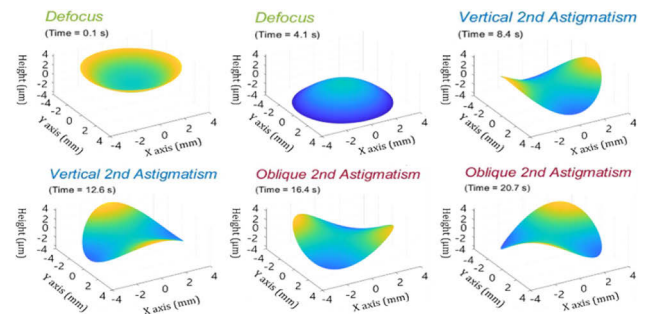


**Fig. 6.** Snapshots of reconstructed wavefronts from the RSWS during temporal sensing tests. During the test run, the DM continuously changed shape. All variations in the wavefront measurements during testing and reconstruction can be viewed in Visualization 1.

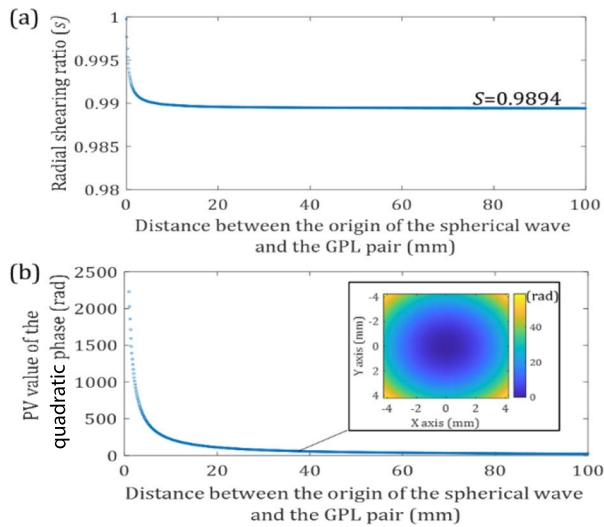


**Fig. 7.** (a) Variation in the radial shearing ratio with  $z_0$  as compared to a system where  $s = 0.9894$  for a flat wavefront. (b) The peak-to-valley (PV) value of the quadratic phase in relation to  $z_0$ .

GPL pair so long as the incident wave remains relatively flat. Once the magnitudes of the incident aberrations are increased, Eq. (4) can no longer be assumed to be accurate. This is true even if the wavefront remains spherical. When this happens, the two output waves from the GPL pair are no longer assumed to be plane waves, leading to the addition of quadratic phase in the image plane.

When a spherical wavefront, instead of a flat one, is incident on the GPL pair, the relative quadratic phase between the two output wavefronts is described as

$$\varphi_{quad} = k(1 - s) \frac{r^2}{z_0}, \quad (5)$$

where  $z_0$  is the distance between the focus point of the incident spherical wavefront and the GPL pair, and  $k$  is the wavenumber. Now,  $s$  can be rewritten to account for  $z_0$  as

$$s = \frac{f - d + fd/z_0}{f + d + fd/z_0}. \quad (6)$$

The radial shearing ratio remains consistent with Eq. (6) as  $z_0$  increases. As shown in Fig. 7(a), the relationship deviates from Eq. (6) when  $z_0$  drops below 10 mm. As shown in Fig. 7(b), even when  $z_0$  is large, the quadratic phase is not zero. To account for this unexpected situation, the quadratic phase is subtracted from the measured phase map to properly reconstruct the wavefront. For example, the quadratic phase associated with  $z_0 = 38$  mm

corresponds to a concave mirror with a 19 mm focal length. When this mirror was measured, the ROC was determined as 49.8 mm instead of 38 mm. Once the quadratic phase was eliminated and the calibration process was complete, the ROC was calculated as 38.1 mm.

In this work, an instantaneous radial shearing wavefront sensor based on the principle of a geometric phase lens pair was proposed and tested. In this sensor, the polarization properties of a geometric phase lens and a polarization pixelated camera are exploited to obtain a phase map with two orthogonally polarized, radially sheared wavefronts. Experimental results from the RSWS were compared to those from a conventional SHWS. Performance tests verified that the RSWS had improved lateral resolution and time-varying response. In order to reconstruct non-planar wavefronts, a calibration of the radial shearing ratio and quadratic phase should be completed as discussed.

**Funding.** Commercialization Promotion Agency for R&D Outcomes (Real-time 3D surface measurement); National Research Foundation of Korea (NRF-2021R1A2C1008661).

**Disclosures.** The authors declare no conflicts of interest.

**Data availability.** Data underlying the results presented in this paper are not publicly available at this time but may be obtained from the authors upon reasonable request.

**Supplemental document.** See Supplement 1 for supporting content.

## REFERENCES

1. M. Nicolle, T. Fusco, G. Rousset, and V. Michau, *Opt. Lett.* **29**, 2743 (2004).
2. E. Savio, L. D. Chiffre, and R. Schmitt, *CIRP Ann.* **56**, 810 (2007).
3. F. Z. Fang, X. D. Zhang, A. Weckenmann, G. X. Zhang, and C. Evans, *CIRP Ann.* **62**, 823 (2013).
4. M. Aftab, H. Choi, R. Liang, and D. W. Kim, *Opt. Express* **26**, 34428 (2018).
5. S. Esposito, E. Pinna, A. Puglisi, A. Tozzi, and P. Stefanini, *Opt. Lett.* **30**, 2572 (2005).
6. D. Wang, Y. Yang, C. Chen, and Y. Zhuo, *Appl. Opt.* **50**, 2342 (2011).
7. M. K. Kim, *Opt. Lett.* **37**, 2694 (2012).
8. Y. B. Seo, H. B. Jeong, H. G. Rhee, Y. S. Ghim, and K. N. Joo, *Opt. Express* **28**, 3401 (2020).
9. T. Ling, D. Liu, Y. Y. Yang, L. Sun, C. Tian, and Y. B. Shen, *Opt. Lett.* **38**, 2493 (2013).
10. D. Bian, D. H. Kim, B. G. Kim, L. D. Yu, K. N. Joo, and S. W. Kim, *Appl. Opt.* **59**, 9067 (2020).
11. L. A. Alemán-Castaneda, B. Piccirillo, E. Santamato, L. Marrucci, and M. A. Alonso, *Optica* **6**, 396 (2019).
12. M. Novak, J. Millerd, N. Brock, M. N. Morris, J. Hayes, and J. Wyant, *Appl. Opt.* **44**, 6861 (2005).
13. W. H. Southwell, *J. Opt. Soc. Am.* **70**, 998 (1980).
14. C. Tian, X. Chen, and S. Liu, *Opt. Express* **24**, 3572 (2016).